Aluminum Bowties for Plasmonic-Enhanced Infrared Sensing

Melissa Najem, Franck Carcenac, Thierry Taliercio, Fernando Gonzalez-Posada

ADVANCED OPTICAL MATERIALS
www.advopticalmat.de

Aluminum Bowties for Plasmonic-Enhanced Infrared Sensing

Melissa Najem, Franck Carcenac, Thierry Taliercio, and Fernando Gonzalez-Posada*

Plasmonic nanoantennas have earned outstanding credits for their powerful ability to couple light from free-space into sub-wavelength-sized structures and to enhance the electric field confinement. One of the most appealing plasmonic applications is biosensing: to detect and identify many bio-information of a molecule in a single test. Consequently, surface enhanced spectroscopy in a broad infrared (IR) range is required. In this article, a barcode-like nanostructured surface of a metal-insulator-metal (MIM) platform serves as optical transducer with tunable localized surface resonances (LSPR). The conception, fabrication, and optical characterization of periodic arrays of aluminum bowties (Al-BT) within a MIM structure compatible with Si-technology are reported. LSPR positions are extended by controlling the side length of the tip-to-tip facing triangles. The reflectance measurements correlate extremely well to numerical simulations. The simulated electrical field confinement provides up to 10^3 of intensity relying on the tip-to-tip nanogap value. Surface-enhanced infrared absorption (SEIRA) gives simultaneously spectral information on both far-field behavior and near-field enhancement of several vibrational lines of our trial molecule (vanillin) achieved with the barcode-like Al-BT. The analysis of Fano-like profiles is concluded with SEIRA enhancement factors higher than 10^7 for frequency tuning ratios below 1 between the far-field plasmonic resonances and the selected vanillin IR absorption lines.

1. Introduction

Plasmonic has become the merging star of nanophotonics and nanotechnology.[1–4] Among its countless applications, biosensing is one of the most engaging as it capitalizes on localized surface plasmon resonance (LSPR) and thus possesses the great advantage of highly-sensitive, label-free, and real-time measurements.[5–10] Indeed, LSPR is more sensitive to the smallest variation in the vicinity of the plasmonic nanostructures, and the smallest footprint compared to the case of commercial propagating surface plasmon (SPP) resonance sensing.[11] Hence, through its ability to investigate single-molecule events in low-concentrations of the target analyte, LSPR paves the way toward the commercial and mass production of nanoresonators integrated on a lab-on-chip, for portable devices and point-of-care diagnosis.[12]

Fundamentally, LSPR arises from the light-matter interaction at the metal-dielectric interface of nanostructures. Due to the symmetry breaking, the SPPs are localized and can be excited and coupled to incoming light with any wave vector k.[13–15] LSPR contributes to a local electromagnetic (EM) field confinement and enhancement in the near-proximity of the nanostructures.[16,17] In analogy to their RF-antennas counterpart, the theory of plasmonic antennas predicts that in the proximity to their sharp edges, the EM field is extremely enhanced and it becomes exceptionally intensified as the resonating nanostructures are closely placed, giving rise to a so-called electromagnetically enhanced hot-spots.[18] Boosting the local EM field enhancement is promising for the probing of any molecule present in the vicinity of the coupled plasmonic resonators, thanks to their high sensitivity to the slightest modification of the surrounding medium refractive index.[19,20] Besides, a ligand-antenna binding is directly translated into a spectral shift of the intrinsic resonance frequency of the antenna in simple transmission, reflection, or scattering measurements. When a ligand infrared (IR) absorption line matches in frequency the plasmonic resonance of an antenna, a Fano-like asymmetric shape appears as witness of the occurring surface enhanced IR absorption (SEIRA).[21,22] Consequently, working in a wide IR range is highly recommended while searching for functional groups and vibrational signatures of any organic compound and living tissue.[23,24]

In addition, plasmonic resonances are deeply sensitive to the material compositions of the nanostructures and their geometry configurations such as the shape, size, and periodicity.[24–26] As an alternative to noble metals, aluminum (Al)

M. Najem, T. Taliercio, F. Gonzalez-Posada
Institute of Electronics and Systems
University of Montpellier
CNRS
Montpellier 34095, France
E-mail: melissa.najem@umontpellier.fr

F. Carcenac
Laboratory for Analysis and Architecture of System
CNRS
Toulouse 31400, France

The ORCID identification number(s) for the author(s) of this article can be found under https://doi.org/10.1002/adom.202201025.

DOI: 10.1002/adom.202201025

has drawn lately great attention for holding attractive features including low cost, high natural abundance, good adhesion to many substrates without the need of any additional layer, as well as flexibility of refinement by various methods including complementary metal-oxide-semiconductor (CMOS) technology.[27–29] Moreover, Al has been largely promoted as it can sustain LSPR from the deep-UV to the IR. Based on this unique characteristic, it can overcome the limitations of Gold (Au) and Silver (Ag). Therefore, Al has a special potential to customize on-demand highly performant refractive index bio sensors,[30–32] surface-enhanced Raman scattering (SERS)[33] and SEIRA platforms.[34,35] Al provides some unique prospects as SEIRA candidate compared to Au antennas, despite the presence of a native oxide layer contributing to greater losses and a more moderate SEIRA enhancement. Precisely, the omnipresent 2–4 nm thick oxide layer, spontaneously formed upon its exposure to the atmosphere, passivates the antenna structure against further oxidation and enables a broader range of covalent binding schemes for molecules to the antenna than Au or Ag.[29]

In terms of geometry, bowtie (BT) shaped antennas are excellent building blocks for engineering tunable LSPR, by varying their triangle side-length and spacing. BTs are exhibiting "lightning-rod effect," as an outstanding E-field is concentrated at their sharp apex.[36,37] This near E-field enhancement is heavily gap-dependent and its energy is qualitatively explained as dipole-like interactions. By decreasing the gaps, a stronger dipole-dipole interaction will lead to an energy reduction, that is a spectral red-shift.[17,37–40] These BTs can be combined within a metal–insulator–metal (MIM) structure which has been recently used as high Q-factor Fabry–Perot resonators.[41,42] The light is confined in the insulator (spacer), leading to this strong light absorption in the structure. The MIM structure has also shown an out-of-plane coupling contribution to maximize the in-plane coupling that generates an E-field enhancement inside the BT gap.[41–44]

In this article, we demonstrate an Al-BT barcode-like of tunable plasmonic resonances to enhance multiple IR absorption lines applied to SEIRA sensing. Optical measurements in the far-field corroborate the near-field simulations precisely. Focal-plane-array (FPA) and single detector Fourier transform infrared (FTIR) measurements were used to demonstrate a SEIRA effect in different plasmonic active zones of the optical sensor transducer. Vanillin (4-hydroxy-3-methoxybenzaldehyde) is our SEIRA test molecule, grown naturally in vanilla beans and chemically synthesized for mass production.[45] It is one of seven phenolic compounds considered for their defensive properties against "hydrogen peroxide-induced DNA damage" in human peripheral blood lymphocytes.[46] Five IR absorption lines of vanillin (C=O, CC, CH, CO, and CH_3) interfere simultaneously within the selected plasmonic resonances of the optical transducer.[47] The overlap between the plasmonic resonances and the vibrational frequencies produces different vibrational signal enhancements coherent with the plasmonic energy of the Al-BT arrays. Considering the active zones for SEIRA, enhancement factors higher than 10^7 are reached nearby the BT inner tips. These promising results introduce a compact, low-cost, and sensitive biosensor to Si-technology.

2. Results and Discussion

Figure 1 illustrates the MIM structure and the design of one zone of BT arrays consisting of equilateral triangles. All the geometrical parameters are denoted in the caption of Figure 1. A 100 nm mirror layer is sufficiently thick to suppress the light transmission in the IR spectral range. The SiO_2 insulator thickness was determined by FDTD calculations to maximize the E-field enhancement in agreement with previous studies of Al and Au BT within a MIM configuration, reference 43 and 41, respectively. The 50 nm top thick layer is a compromise between FDTD reflectance intensity calculation and the technological feasibility to realize a good lift-off after the e-beam lithography. Overall, on the same sensor transducer surface, 17 regions of periodic BT arrays are processed with an area extension of $25 \times 90\ \mu m^2$ and distinguished by the triangle side length L and the gap spacing g. These areas are analytically and experimentally customized, then optically and geometrically characterized. The Al-BT with different side lengths and gaps correspond to a single sensor transducer with nanoengineered surface.

2.1. Nanoengineering of the Sensor Transducer Surface

The combination of electron beam lithography (EBL) and lift-off technologies demonstrates a controllable and reliable fabrication

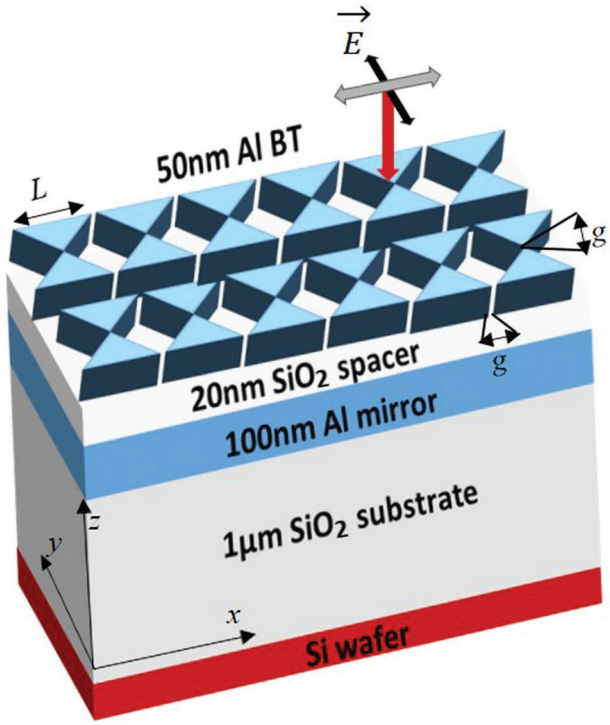

Figure 1. Schematic of the BT nanoantenna arrays integrated in a MIM sandwich structure (Al-BT (50 nm)/SiO_2-spacer (20 nm)/Al-mirror (100 nm)), stacked on a MOS-compatible substrate (SiO_2/Si). L is the equilateral triangle side length of a BT; g is the tip-to-tip and corner-to-corner gap. Each BT is considered as an FDTD unit cell and the periodicity is defined by the boundary conditions. Red, black, and grey arrows illustrate, respectively, the wavevector of the incident-light, the co-polarized electric field (parallel to the BT main axis), and the magnetic field directions.

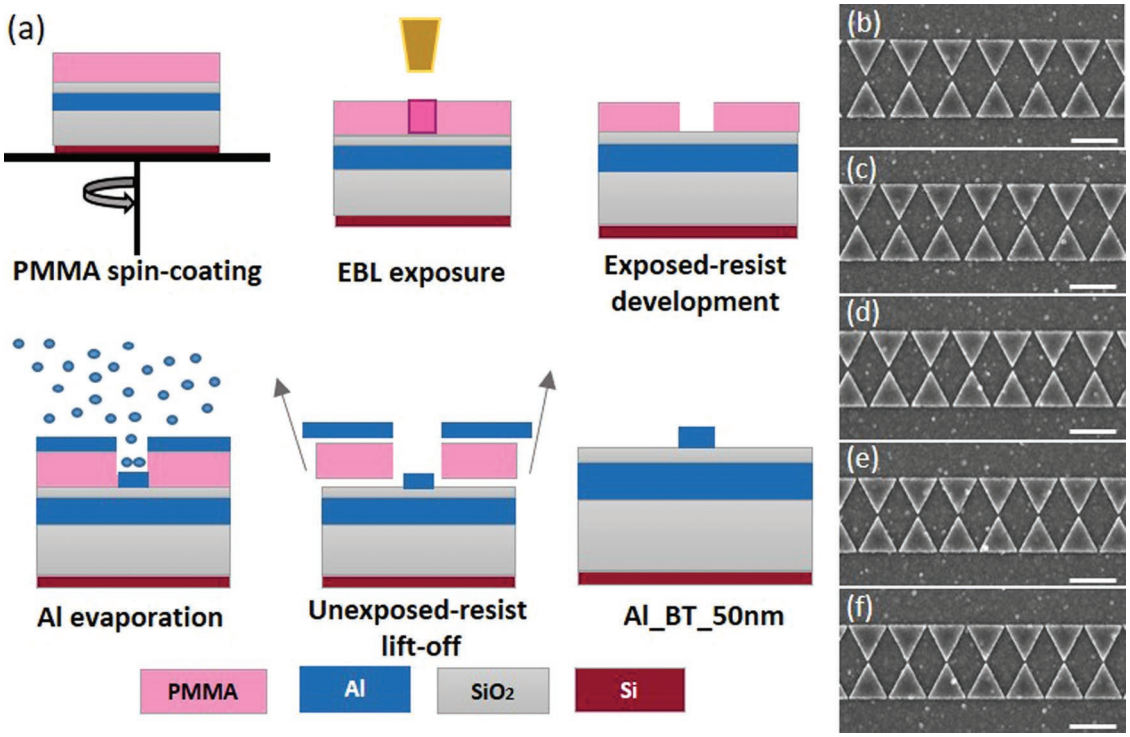

Figure 2. a) Technological process-flow starting with i) PMMA resist spin-coating, followed by ii) an EBL exposure and iii) a standard development, then iv) a metallization and ending with v) a lift-off process, to retrieve vi) the final Al-BT. b–f) SEM images of the fabricated BT, L equals to 0.8 µm, and g is varying from 100 nm down to 20 nm with a step of 20 nm. All scale bars are 1 µm long.

process of Al-BT with nanogaps. The fabrication steps are represented in **Figure 2**a: i) Positive tone resist spin-coating, ii) EBL exposure, iii) exposed-resist development, iv) e-beam evaporation of Al, v) unexposed-resist lift-off, and vi) the final structure of 50-nm-thick Al-BT. Figure 2b–f are SEM images of the periodically lithographed BT arrays with a $L = 0.8$ µm, featuring variable gap values, which are progressively decreasing from 100 nm to 20 nm with a step of 20 nm. The gap separations g are 99.0 ± 2 nm, 81 ± 4 nm, 61 ± 4 nm, 38 ± 5 nm, 22 ± 3 nm, respectively, measured in a collection of 5 SEM images of 5 × 7 BT antennas for each zone. According to all collected SEM images, the corners angle and the triangle side length are respectively equal to 59.6 ± 0.2° and 0.799 ± 0.002 µm. The pitches along x-axis, Λ_x, are also measured and their respective values are 0.902, 0.883, 0.862, 0.847, 0.825 ± 0.002 µm. Substantially, Figure 2b–f highlights only a sampling of the high control achieved on the geometric parameters which are tailored at the nanoscale. Remarkably, the constructed triangles are equilaterals, manifesting finely-sharp and well-defined edges, despite the whole process limitations starting from the control of the multi-stacked layer deposition, followed by a relatively critical EBL writing over a large area, ending with a nanoscale features lift-off step. In sum, the measured values on the whole optical transducer surface are found to be in high conformity with the expected parameters, as confirmed also by the following optical characterizations.

2.2. Optical Characterization

Figure 3 shows reflectance spectra in a wide spectral range from the mid-IR to the near-IR using a single optical transducer surface. The LSPR wavelength is tuned over a wide IR spectral region, from 1000 to 10 000 cm^{-1}, thanks to the size of the Al-BT in each zone of arrays. The BT geometry affects the plasmonic behavior systematically. Fundamentally, for each couple length and gap for the BT, (L and g), a unique LSPR peak is assigned. For this wide-coverage in the IR, L is varied from 0.3 to 2.0 µm with a step of 0.1 µm, and g is swept from 100 nm down to 20 nm with a step of 20 nm. The distance between the antenna rows, Y, is maintained constant at 2 µm. The BTs are illuminated under co-polarized light (E-field parallel to the BT main axis), which provides an effective facing tip-to-tip coupling and supports high field enhancement into that gap. Figure 3a shows the experimental reflectance spectra of each structured zone under a microscope coupled to a FTIR spectrometer using a single element MTC detector. For all BT regions, the first-order plasmonic resonance is always situated at the lowest wavenumber (that is lowest energy) and then higher orders of the resonance appear at higher wavenumbers. As the BT sizes increase (L increases), the main LSPR peaks are gradually losing energy from 8300 to 1500 cm^{-1} (red shifting from 1.2 to 6.5 µm). This behavior corresponds to the dipolar mode which demonstrates a wavelength shift as L varies. This well-known tendency for metallic objects is largely described in the literature.[18,25,26] Some higher-order radiative (bright) modes are visible only for $L > 0.9$ µm with a similar tendency. An extensive analysis of all these modes in regards to the IR light polarization will be the subject of a forthcoming work. Figure 3b represents the numerical results calculated using FDTD simulations. Similarly, one main resonance peak is attributed to each L value. Accordingly, LSPR peaks are shifted toward a lower wavenumber as L is increased. Furthermore, the

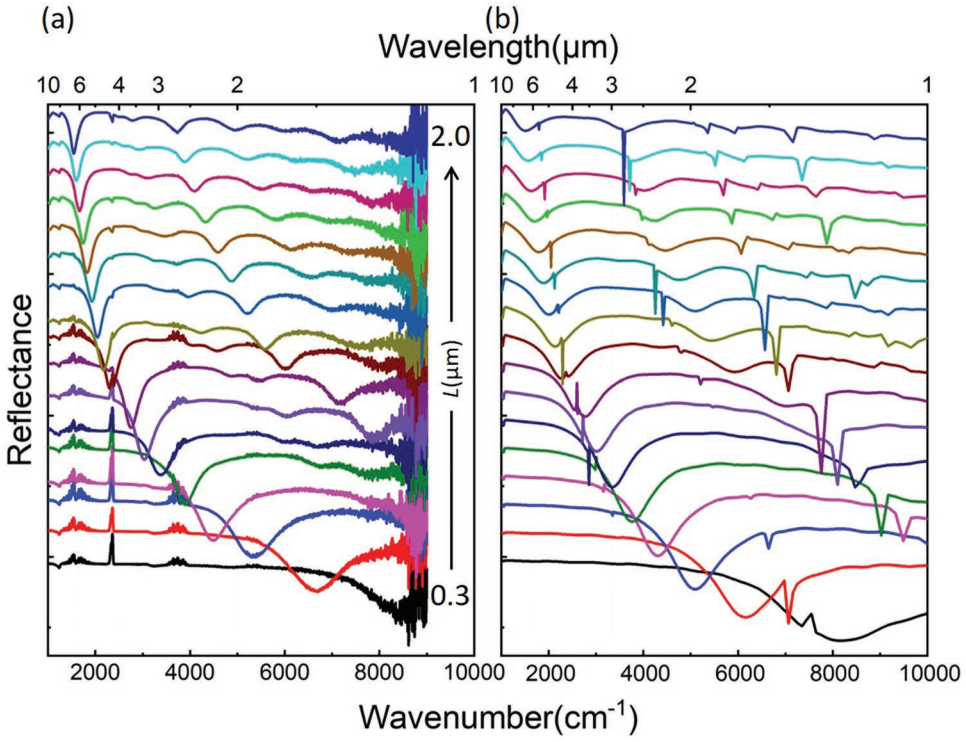

Figure 3. Optical transducer plasmonic modulation over a wide range in the IR according to the side length of the BT in each array zone. a) Experimental (FTIR) versus b) numerical (FDTD) reflectance results for BT arrays illuminated under co-polarized light (E-field parallel to the BT main axis), where *g* is kept constant at 100 nm and *L* is varying from 0.3 to 2 μm with a step of 0.1 μm. Note the spectra are stacked along the reflectance axis for ease of viewing.

simulated peak widths decrease continuously along with the simulated spectral range as the peak shifts to lower energies, likewise for the experimental ones (Figure 3a), agreeing with the state-of-art.[48] The agreement between numerical and experimental results is almost perfect. Despite their resemblance, the numerical results show well-sharp peaks identified as BT array's diffraction peaks resulting from the periodicity which is triggered along the *y*-axis. Their spectral position, Λ_y, has been analytically deduced for equilateral triangles as Equation (1) is fulfilled:

$$\Lambda_y = 2 \times L \times \sin 60° + g + Y \quad (1)$$

However, these spiky diffraction peaks are latent under the FTIR detector having a wide NA objective in the microscope. Moreover, in Figure 3a the surrounding environment concrete effects are observed since the optical measurements are acquired in an N_2 medium and not in vacuum. Indeed, absorption lines of water and CO_2 are manifested in the FTIR results. In Figure 3a, the signature of weak oscillations spanning between 1090 and 1800 cm^{-1}, 3500 and 3900 cm^{-1}, and above 5000 cm^{-1} corresponds to water lines. In contrary, the ro-vibrational modes of CO_2 are concentrated around 2350 cm^{-1}.

The combination of focal plane array (FPA) detectors to conventional FTIR systems allows a concurrent and rapid collection of thousands of infrared spectra over large areas of a sample, which has been particularly useful in surface chemical analysis.[49–51] **Figure 4** presents the high potential of the FPA to detect geometry differences at the nanoscale range on a nano-engineered surface with multiple BT array's zones. Figure 4a is a real shot of the sample surface with two different triangle sizes, $L = 0.8$ μm and $L = 0.9$ μm, and 5 gaps from 100 to 20 nm with a step of 20 nm, with colored-pixels and indexed by the *L* and *g* values corresponding to each zone. Figure 4b represents the reflectance spectra of only two single pixels (2×2 μm^2) on each BT array zone showing the effect of *L* on the LSPR position and a pixel on the bare substrate. Figure 4c is the so-called pixelated surface chemical image showing a color contrast between different BT arrays zones. The contrast is defined by the hatched areas of the integrated zone in Figure 4b. The integration area is delimited by the spectrum curve and black lines drawn between the intensity (reflectance) values of the two pre-defined wavenumber limits (gray dashed lines). The hatched areas of Figure 4b contain the spectral intensity of each detected pixel within the selected wavenumber range. A larger area implies a stronger activation of the pixel in the integrated zone. The numerical treatment in a pre-defined integrated zone of all the pixels (340×340 μm^2) is translated by a color-coded pixel's excitation for the involved hatched area as shown in Figure 4c. The contrast intensity (color scale of Figure 4c) is strongly negative whenever the hatched zone is situated below the straight black line of the integration, and it is positive in the opposite case. As the integration area in Figure 4b is encompassing a notable part of BT arrays with $L = 0.9$ μm resonances, and the hatched area is largely situated below the straight black line, the boxes of those BT arrays are mainly activated in dark

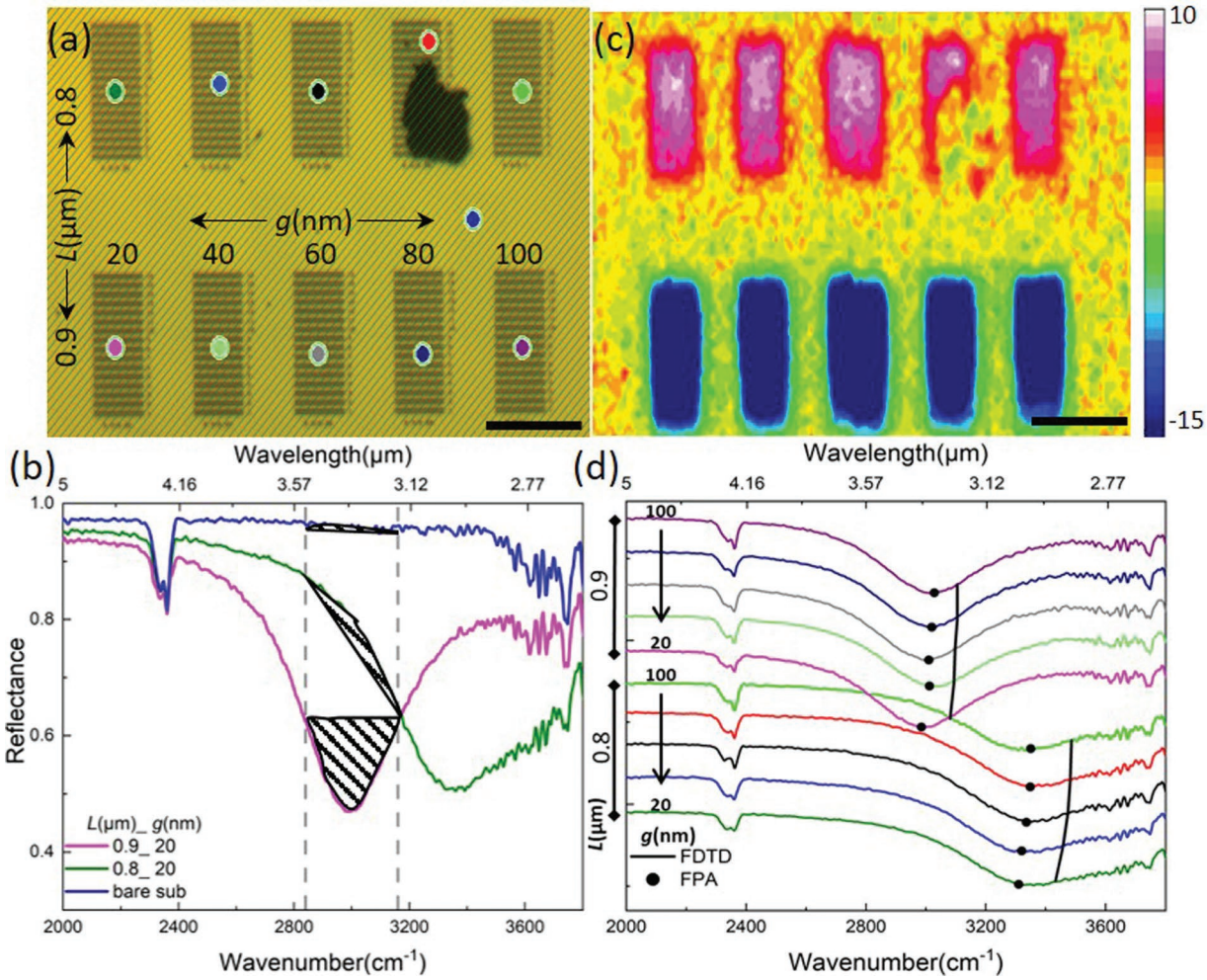

Figure 4. Surface response investigation of BT arrays with $L = 0.8$ and 0.9 μm with variable gap values under focal plane array detector. a) Real image of the sample with colored pixels for each L (μm) _g (nm) fixed couple, b) for $g = 20$ nm, plasmonic resonances ω_{res} of BT arrays with $L = 0.8$ and 0.9 μm are centered in 2.95 and 3.32 μm, respectively; after the integration of the hatched areas (c) is the activated color-coded chemical image; d) spectra plotted in stack for all the colored pixel of (a) showing theoretical (lines) versus experimental (dots) results. All scale bars are 50 μm long.

blue in Figure 4c, while those of $L = 0.8$ μm, are less activated and represented in pink (positive contrast as the hatched area is above the straight black line), and the bare substrate is mainly activated in yellow (intensity near 0) as the involved area is negligible. Figure 4c digitalizes the authentic homogeneity of the fabricated surface and reveals real defect areas on the sample surface as observed in the BT array zone corresponding to $L = 0.8$ μm and $g = 80$ nm through pixels disarrangement, corresponding to the dust in Figure 4a. Finally, in Figure 4d, the reflectance of each colored-pixel of Figure 4a stacked together highlights the gap effect on the LSPR position for the BT arrays with a constant L. A similar effective energetic displacement of the LSPR positions is measured, following the black dots labeled FPA, and simulated, following the black curves labeled FDTD. Both tendencies agree with the previously-cited coupling theory.[33] Though, a slight spectral shift is separating the FTIR-resonance positions and the ones retrieved by FDTD. Actually, in FDTD the materials are usually pre-defined in perfect conditions. Even though some modifications could be applied to match the concrete quality of the deposited materials, such tangible mismatch (not only counting the material optical properties but also the surface oxidation and roughness) is displayed in a collective redshift of the experimental results compared to the analytical ones.[52]

2.3. Local Field Enhancement

In addition to their behavior in the far-field, BT arrays resonances are accompanied by an outstanding near-field feature to localize and enhance the E-field at the nanoscale between each triangle of the BT array.[16] In fact, the interaction between the oscillating charges on two sharp-and-aligned structures becomes more significant as soon as they come closer to each other, thus creating a hotspot. Accordingly, under a co-polarized light, the near electric field (E-field) enhancement and intensity are boosted inside the gap which is formed between the sharp-ends of both coupled triangles that are facing each other. Here, for a finer resolution, the mesh override pitch is reduced to 2 nm to illustrate the E-field dependency on the

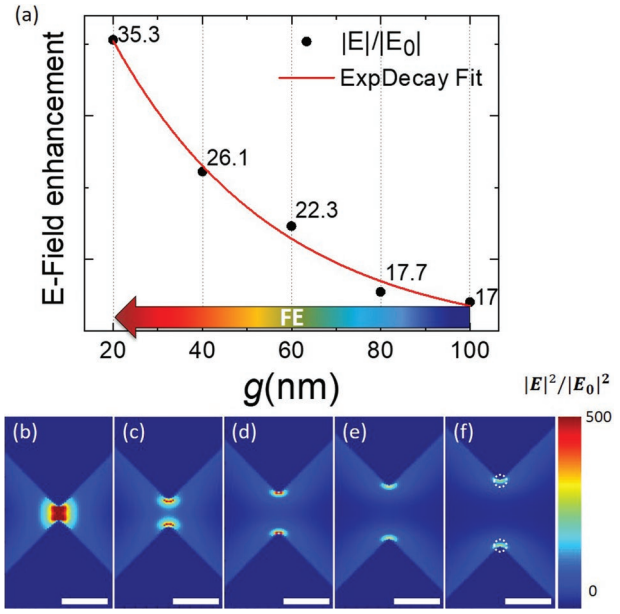

Figure 5. Gap value influence on the local field enhancement and intensity for L = 0.8 µm with g ranging from 100 to 20 nm with a step of 20 nm. a) E-field enhancement $|E|/|E_0|$ in function of the g exponentially decaying as g increases (red curve), along with the associated enhanced electric field mapping (b–f) calculated at 2.96 µm and acquired under co-polarization. The color scale ranging from blue to red indicates the minimum to maximum field intensity $|E|^2/|E_0|^2$, max ($|E|^2/|E_0|^2$) equals 1250, 700, 500, 315, 300 for mapping from (b)–(f). For better contrast, the maximum of the color scale is fixed at 500. All scale bars are 100 nm long. The dotted circles, with a radius of 8 nm, are denoting the active area for the upcoming SEIRA investigation.

gap value. Based on the graph in **Figure 5**a, the local E-field is intensified at the tips and its enhancement $|E|/|E_0|$ is increasing exponentially (red curve showing an exponential fit) while gradually decreasing the tip-to-tip gap value from 100 nm to 20 nm. Its intensity $|E|^2/|E_0|^2$ is increasing too as far as the tip-to-tip spacing decreases which agrees with the statement that the coupling between two sharp extremities over a narrow gap can create highly-localized and strongly-enhanced near E-field. Figure 5b–f shows the E-field distribution in the xy-plane into the tip-to-tip gap region while increasing its intensity value respectively from 20 to 100 nm based on the accompanying color scale. Even though decreasing the gap value will engender a slight red-shift according to the inter-triangle coupling principle, macroscopically, the LSPR peak position is nearly situated around 2.96 µm. At such a wavelength, $|E|^2/|E_0|^2$ rises from 300 to around 1250 as the gap value decreases.

Inside a gap of 20 nm (Figure 5b), the near E-field is intensified in a circular shape around each of the tip-to-tip sharp extremities. Hence, the radius of each circle, R, is fittingly assumed to be equal to 8 nm. Such localization is replicated despite the gap value (Figure 5b–f), and symbolized by a dotted white circles in Figure 5f. This numerical observation is extremely necessary for the forthcoming SEIRA demonstration that is mainly arising from the interaction between the deposited molecules and the intensified near E-field owing to the lightning-rod effect.

2.4. SEIRA Sensing Investigation

To evaluate SEIRA spectroscopic features, vanillin is dissolved in ethanol with a concentration of 2 mg ml^{-1}. Then, a droplet of 1 µL is deposited on the plasmonic transducer. Around 10 nmol are hence released on the whole sample surface, the molecular mass of vanillin being 152.1 g mol^{-1}. The adsorption of vanillin on Al follows a Langmuir isotherm model: the adsorbed molecules do not interact and the energy of adsorption is equivalent for all sites, hence, each of which can hold at most one molecule. In this sense, a mono-layer coverage could be assumed once the vanillin is placed on the Al-BT surface.[53] Thus, the distribution of vanillin molecules is supposed to be homogeneous on the sensor transducer surface of approximately 1 cm^2. Accordingly, 0.4 nanograms of vanillin are located within the zone of 230 × 90 µm^2, where 5 zones of Al-BT arrays are designed in areas of 25 × 90 µm^2 each, separated by 25 µm, with the same length, L, and five different gaps, g (see the red square in **Figure 6**a,d as an example).

To evaluate the immediate surface sensing, FPA would be a challenging but compelling method to attempt, more concretely thanks to its chemical image treatment under a 15× IR objective, 100 scans with 4 cm^{-1} of resolution are selected to collect the most reliable spectra as the vanillin/ethanol droplets are time-sensitive.

Figure 6a,d is the real image of the sample zone consisting of BT with L equals to 2.0, 1.9, and 1.8 µm, before and after the deposition of vanillin/ethanol droplets. The assumed homogeneous distribution of vanillin molecules is experimentally demonstrated in Figure 6d (small roundish spots). Each colored dot is selected for a gap value. A reflectance collection for three gap values is respectively plotted in Figure 6b,e. For further investigations, purple and magenta dots are selected as reference to the bare substrate and the spot of vanillin molecules, respectively. For all the plasmonic areas, the spectral resonances redshift ≈ 40 cm^{-1} in presence of vanillin/ethanol solution, as found by comparing Figure 6b,e. In other words, the SPR sensing is noticed directly by the FPA in each pixel with a sensitivity ≈ 185 nm/RIU (≈ 10^2 as reported by Mayer et al. for metallic nanoparticles).[19] Moreover, in Figure 6e, the absorption signatures appearing at 1509, 1587, and 1665 cm^{-1}, correspond to certain vibration frequencies of vanillin (gray lines). Indeed, the modifications in the reflectance spectra, that is, the Fano-like asymmetric features of the SEIRA sensing, correspond to the perfect spectral match between Al-BT resonances and several vibration frequencies.

Therefore, FPA offers a unique advantage to assess qualitatively the SEIRA activation. In Figure 6b,e, an integration zone (delimited within dashed blue lines) is framing the absorption signature of vanillin situated at 1509 cm^{-1} that matches the plasmonic resonance of L = 2.0 µm. Consequently, in Figure 6c, the boxes of BT arrays with L = 2.0 µm are mainly activated in dark blue, while those of L = 1.9 and 1.8 µm, are less activated and represented in cyan blue. In Figure 6f, the SEIRA signature integration is promisingly pronounced onto the BT arrays zones, where small red spot areas show a high contrast in comparison to the large green ones. This color activation underlines the aptitude of the tailored tip-to-tip plasmonic BT to indicate a location of the arising SEIRA.

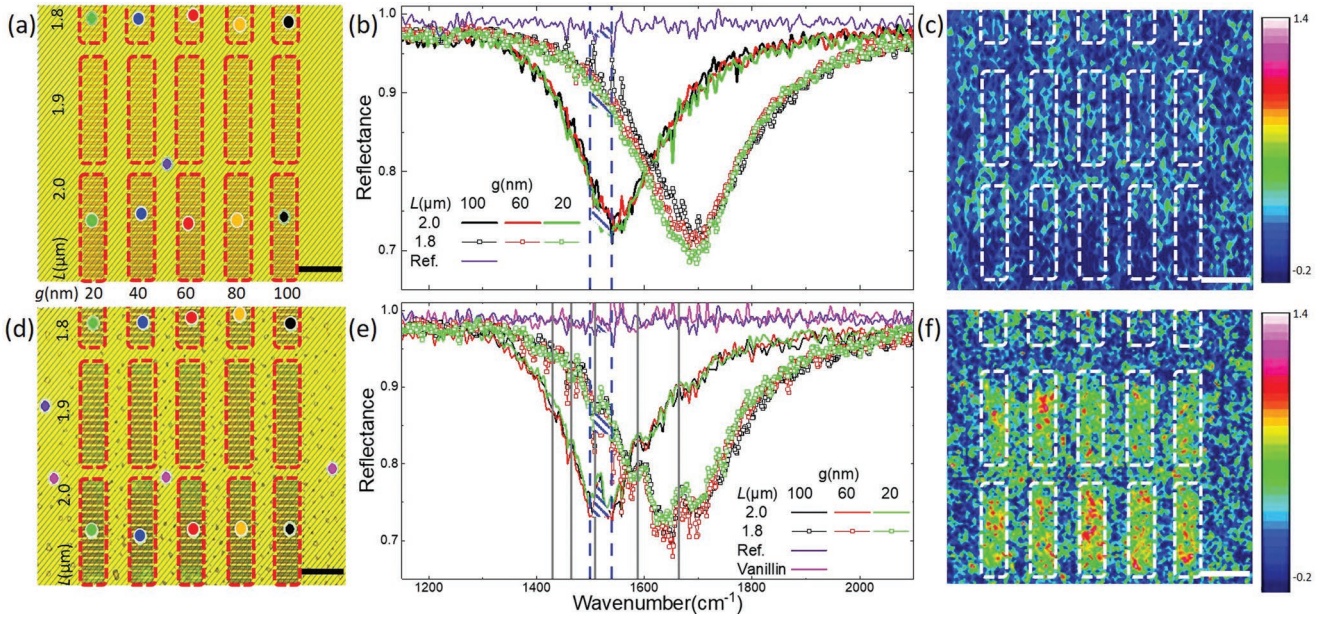

Figure 6. Surface response investigation under a co-polarization of BT arrays with L = 2.0, 1.9, and 1.8 µm with variable gap through focal plane array detector. a–c) The results before vanillin deposition, and d–f) the inquiry after vanillin deposition. a,d) Real images of the sample with color pixels for each gap value. Purple and magenta dots stand for bare substrate and vanillin spots, respectively. A homogeneous coverage is illustrated in (d). Plasmonic resonances are collected pixel by pixel and represented in (b,e) for the color-corresponding BT as well as for the vanillin spots (magenta) and the bare substrate spots (purple). The resonances in (e) are redshifted in comparison to (b) and the Fano-line shape of the vibrational features spectrally covered by the broad LSPR evidences the coupling between the LSPR and the narrow vibrational lines, through asymmetric features (gray lines). The hatched areas around an absorption line of vanillin show the contrast of amplitude between both resonances without and with vanillin, then the color-coded chemical images (c,f) are activated after integration (dashed blue lines), highlighting the induced SEIRA that is mainly arising from the BT arrays. All scale bars are 50 µm long.

The near-field theory presented in the mappings of Figure 5 demonstrates the influence of the gap value on the electrical field enhancement and consequently on the expected SEIRA effect. The highest electric field enhancement corresponds to g = 20 nm, and therefore it is the most sensitive to the surrounding molecules. However, the corresponding ω_{res} should imperatively be finely tuned to be suitable to produce the strongest intended S-shape profile. In Figure 6f, the red spots can be identified as the strongest enhancement sites of the signal corresponding to the vanillin line situated at 1509 cm^{-1}, around which the integration is done in Figure 6e. Thus, for a 60 nm gap value the spectral overlap between the ω_{res} and ω_{vib} seems to be perfectly adapted to produce a strong enhancement of the pre-mentioned absorption line. Indeed, as demonstrated in Figure 4d, the ω_{res} decreases when decreasing the BT gap value. These spectral shifts due to the gap variation affect the SEIRA study in function of the gap size for the same BT length. A quantitative analysis of the SEIRA effect can be done by comparing Figure 6b,e using the spectrum of single pixels of the FPA. However, the amplitude resolution of the absorption signatures is limited due to a low signal-to-noise ratio (SNR) of the FPA spectrum of single pixels in these measurement conditions. Besides, the strengths of the resulting asymmetric lines are challenging to analyze, and the influence of the gap variation makes it tough to deduce the most adequate BT gap to perfectly trigger the selected absorption line.

To overcome the low SNR of FPA, complementary far-field measurements are done using the single element detector under a 36× IR objective (NA = 0.5). The reflectance area of the optical transducer is selected by a manual knife-edge aperture corresponding to only 5 zones of Al-BT of the same length with different gaps sizes from 20 to 100 nm. **Figure 7** presents the performed reflectance measurements on the same sample position without (Figure 7b) and with (Figure 7c) the vanillin/ethanol (2 mg ml^{-1}) droplet and the retrieved vibrational signals (Figure 7d). Figure 7a gives a reference for the vanillin absorption lines from 1100 to 2100 cm^{-1}, obtained from a transmittance measurement of a highly-concentrated vanillin solution (50 mg ml^{-1}) in ethanol, deposited on an IR-transparent KBr crystal. Below 1400 cm^{-1}, the IR absorption lines of the vanillin are not accessed (Figure 7c). However, five narrow IR absorption lines of the vanillin for wavenumbers higher than 1400 cm^{-1} are interfering within large plasmonic resonances, corresponding to Al-BT arrays of L from 2.0 to 1.4 µm with a step of 0.1 µm. The five absorption features of vanillin are situated at 1430, 1464, 1509, 1587, and 1665 cm^{-1} (see the vertical gray lines along Figure 7). These lines correspond closely to C=O, CH, CC, CO, and CH_3 stretching, in-plane bending and asymmetric deformation vibrational lines.[47] The experimentally found vibrational lines are slightly shifted compared with the analytical ones in reference 47, due to the interaction of the molecules with the substrate and their medium (solid, liquid) which is directly affecting their binding energy. For each of these five IR lines, asymmetric line shapes (Fano-type) highlight the corresponding hybrid coupling between large plasmonic resonances ω_{res} and narrow vibrational mode ω_{vib} frequencies (Figure 7c).

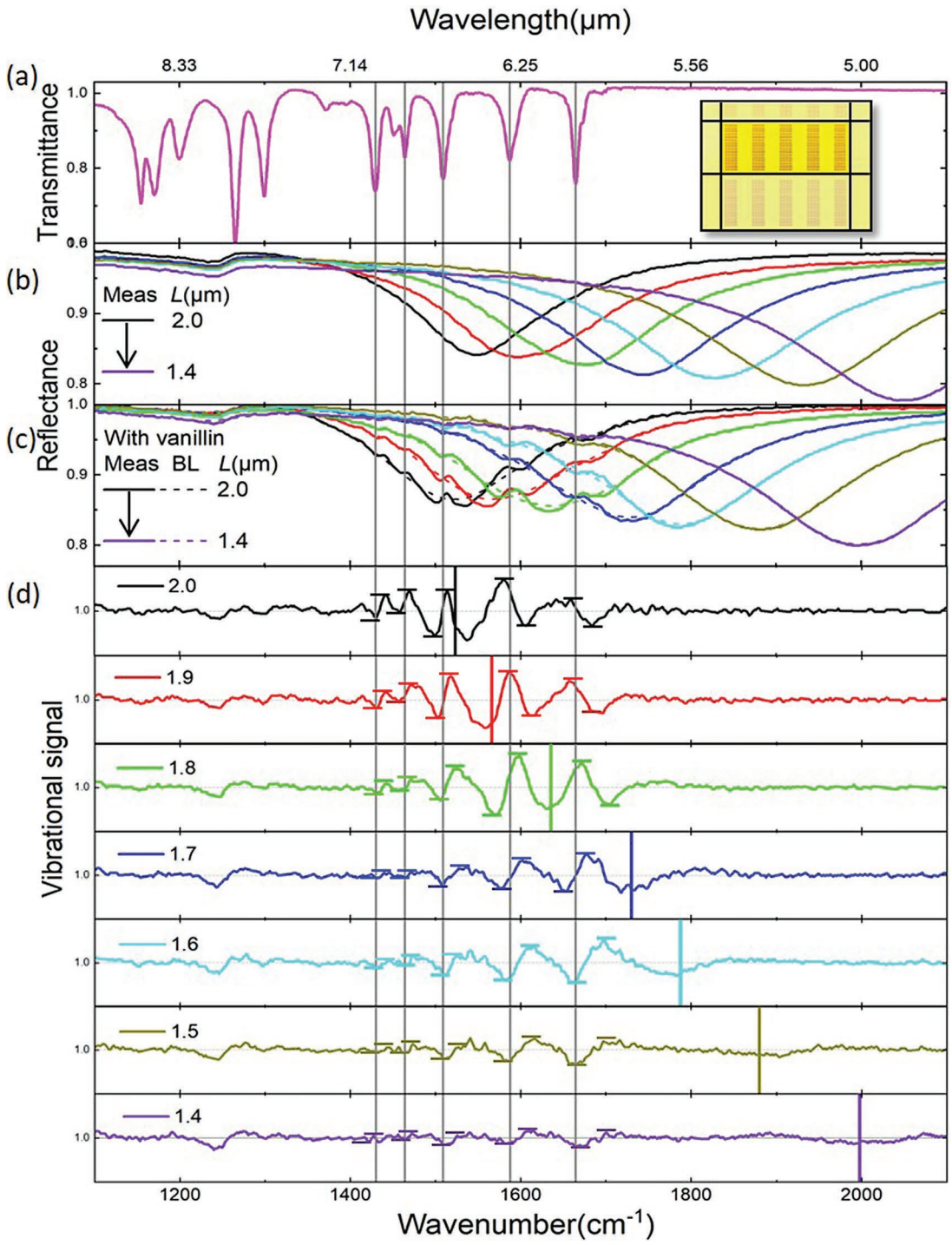

Figure 7. Resonant SEIRA sensing demonstration of vanillin using Al-BT. a) Transmittance spectrum of vanillin (50 mg mL^{-1}) normalized to the one of cleaned KBr platelet, shown as reference. Gray vertical lines eye-guide the IR absorption lines of vanillin. The inset shows an FPA image of the five zones of Al-BT selected by a manual knife-edge covering 230 μm × 90 $μm^2$. Reflectance spectra of the Al-BT of different side lengths L varying from 2.0 to 1.4 μm with a step of 0.1 μm, covering accordingly a wide spectral range from 1400 to 2100 cm^{-1} are acquired before (b) and after (c) the deposition of vanillin. The dashed curves are the corresponding baseline (BL) fitted using Eiler's smoothing algorithm, excluding the vibrational features (Fano-type).[54] d) Vibrational signals normalized by the BL for each BT arrays (side length L given in microns). The plasmonic resonance positions ω_{res} are marked with thick colored vertical lines. The signal strengths of the enhanced molecular vibrational modes (S-shape) are obtained as a peak-to-peak value, delimited by the horizontal ticks. Note the signal strength and the line shape changes with respect to ω_{res}.

In Figure 7d, the vibrational signals are obtained by the normalization of the reflectance for each BT array to the baseline (BL, dashes lines in Figure 7c) calculated by Eiler's least square smoothing algorithm.[54] This hybrid coupling efficiency is

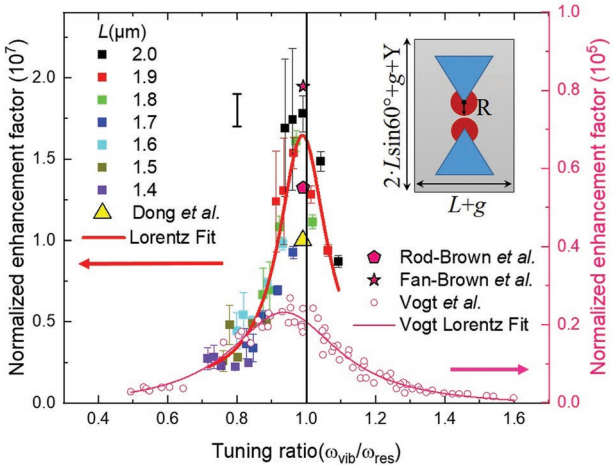

Figure 8. Normalized enhancement factor (EF) of the five enhanced absorption modes of vanillin in the considered spectral fingerprint range versus the ratio of molecular and plasmonic resonance frequencies ($\omega_{vib}/\omega_{res}$). The inset shows the A_0 and A_{SEIRA} with a 100 nm gap for all the BT arrays of the same length. The vibrational signal enhancement is generally maximized below $\omega_{vib}/\omega_{res} = 1$ (black line) as found with a Lorentz curve (thick red curve), declaring the perfect overlap between vibrational modes and plasmonic resonances. The thick error bar represents the systematic error related to A_{SEIRA} estimation, to be introduced to the maximum EF value. Vogt et al. data is plotted in pink circles as well as their Lorentz fit (thin pink curve). For further comparison, Brown et al. and Dong et al. data are plotted as specific symbols (see the legends). Note the difference of the *y*-axes scales corresponding to each legend.

interpreted through the strength (peak-to-peak value) and the shape of the Fano-like signals and is modulated by a tuning ratio $\omega_{vib}/\omega_{res}$. As plotted in Figure 7d, when $\omega_{vib}/\omega_{res} \approx 1$ (typically around the colored vertical lines), the vibrational signal strength tends to have a higher peak-to-peak value for the different L values, stating the best spectral overlap between ω_{vib} and ω_{res}. The vibrational signal shapes are also impacted by the tuning ratio. For example, selecting $\omega_{vib} = 1665$ cm^{-1}, for coupling tunings above 1 (red Fano), the line shape keeps on the conformist asymmetric outline but with inverted minimum and maximum compared to tunings below 1 (blue Fano).[55]

To evaluate the SEIRA sensitivity of the Al-BT arrays, **Figure 8** summarizes the enhancement factor, EF, for the five IR lines of the vanillin according to the spectral tuning ratio. EF is defined by the expression of Equation (2) as:

$$EF = \frac{S_{SEIRA}}{S_0} \times \frac{A_0}{A_{SEIRA}} \tag{2}$$

where S_{SEIRA} and S_0 are the enhanced and unenhanced signal strength, respectively. From the measurements on a metallic surface, the unenhanced signal strengths, S_0, are found in the order of $2–5 \times 10^{-3}$ for the absorption lines. The signal strengths of the enhanced molecular vibrational modes (S-shape) are obtained as a peak-to-peak value, delimited by the horizontal ticks. The signal strengths, S_{SEIRA}, are in the order of 2×10^{-2}, as measured in Figure 7. A_{SEIRA} and A_0 denote the areas covered with molecules in SEIRA and the reference measurements, respectively (see the inset in Figure 8). The A_0 is defined in analogy to the FDTD unit cell, that is the repetitive surface accessible to the molecules at the BT surface. The surface is analytically calculated as developed in Equation (3):

$$A_0 = \left(2 \times L \times \sin 60° + g + Y\right) \times \left(L + g\right) \tag{3}$$

In the following, the gap is considered equal to 100 nm for the 5 zones as the worst-case scenario for a low near-field enhancement, regarding the mapping of Figure 5. The total antenna surface area, A_0, yields 0.4 picograms per BT antenna. For a completely covered antenna, 15×10^8 molecules per BT antenna are expected. However, the probed molecules are traced in the antennas intense near-field hotspots, specifically at the sidewalls of the activated tips (see Figure 5f). As the SEIRA signal originates essentially from these molecules, an effective area, A_{eff}, that is accessible to the analyte is defined as the 5/6 of an 8 nm-radius circular surface centered around the BT tip, where the local EM field is intensified, excluding thus the internal area of the equilateral triangle tip. Under a co-polarization, as the E-field is localized and enhanced at both inner BT tips, A_{SEIRA} is counting twice the A_{eff}. A_{SEIRA} represents 0.04 % of the unit cell area A_0. Therefore, 5×10^4 molecules are located at both inner tips (A_{SEIRA}), hence, approximately 2.5×10^4 molecules per tip (A_{eff}). The number of molecules is three orders of magnitude lower than the value reported by Barho et al. for vanillin detection ($\approx 5 \times 10^7$ molecules per antenna) with highly doped semiconductor periodic rectangular nanoantenna arrays, where the E-field is only localized at the resonator corners. Interestingly, this number of molecules is in the same order of magnitude as the best-reported values so far for the detection of self-assembled monolayers (SAM) of stearic acid (also known as octadecanoic acid) using asymmetric Al cross-antennas ($\approx 3.6 \times 10^4$ molecules at the tip region of the antenna) and octadecanethiol (ODT) with a gold nanorod antenna ($\approx 1.5 \times 10^4$ molecules per antenna), respectively reported by Halas et al.[29] and Neubrech et al.[17] Furthermore, using a MIM structure with Fan-like Au nanoantennas in a 3×3 array, Brown et al. achieved the detection of $\approx 0.5 \times 10^4$ molecules par antenna of ODT,[22] and Dong et al. detected ≈ 500 molecules of 4-nitrothiophenol per antenna.[56]

Subsequently, Figure 8 shows the evolution of the normalized enhancement factor EF versus the ratio of molecular and plasmonic resonance frequencies $\omega_{vib}/\omega_{res}$. EF is established in respect to the signal strength and the active area of BT arrays from $L = 1.4$ to 2.0 µm. The order of magnitude of the EFs is $\approx 10^7$ as shown in the *y*-axis of Figure 8. Typical EFs stated in the literature according to Neubrech et al. are ranging from 10^3 to 10^5 depending on the antenna shape, material, and organization.[17] The EF maximum value is 1.8×10^7 found for a tuning ratio $\omega_{vib}/\omega_{res} = 0.99$.Thus, the strongest enhancement is achieved for the absorption line ω_{vib} situated at 1509 cm^{-1} with a BT array of $L = 2.0$ µm, resonating at a $\omega_{res} = 1524$ cm^{-1}. It is four order of magnitude higher than the reported value by Vogt et al. for IR sensing (EF $\approx 10^3$ using Au nanorods).[55] Furthermore, the data of Vogt et al. are plotted on the same graph (pink circles) to underline the improvement of the EF achieved using Al-BT as well as their constantly global tendency to be maximized for $\omega_{vib}/\omega_{res}$ below 1 as fitted by a Lorentz curve (thick red curve) with a maximum centered around 0.98 and 0.16 as full width at half maximum (FWHM). This result agrees well

with the fact that the optimal enhancement is established at a tuning ratio slightly lower than 1 between the vibrational line and the antenna plasmonic resonance frequencies, consistently with Wallace et al. SEIRA measurements of 4-nitrothiophenol-functionalized gold dendritic fractals,[57] and Vogt et al. findings (see in Figure 8 the Lorentz fit with a thin pink curve).[55] The smaller FWHM indicates less losses and consequently a higher EF, and it is most probably due to the high energy confinement within the Al-BT MIM configuration as well as to the reduced effective area of the near E-field distribution compared to the previously mentioned Au nanorods. Finally, in Figure 8 the EFs are similar to the values reported by Dong et al.; with a 3-nm gap MIM BT antennas.[56] However, the resulting EFs are two order of magnitude higher than those reached with 20-nm gaps Fan-like Au nanoantennas with MIM structures, as reported by Brown et al.[22] This difference of the EF values is attributed to a larger E-field confinement gained thanks to the reduced thickness of the SiO_2 insulator layer (20 nm), creating thus a gap-plasmon effect, in comparison to their ≈ 300 nm insulator layer, defining an optical cavity.

The influence of both near-field enhancement and far-field energy shift on the SEIRA signal enhancement is experimentally demonstrated under a co-polarized light. Similar results could be found under a cross-polarized, for an electric field oriented perpendicularly to the BT main axis. Based on the enormous E-field enhancement obtained for small gaps (Figure 5), the gap influence on the SEIRA enhancement will be the subject of an upcoming study where larger nanoengineered areas of 100×100 μm^2 with variable gap values are approached to compensate the low signal-to-noise ratio (SNR) achieved following the compromised FPA parameters and due to the characterization of small tailored zones (25×90 μm^2).

3. Conclusion

In summary, we have defined a well-controlled procedure for creating a multi-resonating optical transducer of Al-BT using electron-beam lithography and lift-off technique. The influences of geometric parameters of Al-BT, that is, the size and the gap spacing were studied in detail. The far-field resonances of Al-BT integrated to a MIM have been numerically modeled and experimentally proved. Good agreement was found between both approaches. The triangle side length effect on the LSPR resonance was carefully supervised and has shown a redshift of the LSPR while increasing *L*, leading by this to a wide coverage of a broad IR spectral window from 1500 to 8300 cm^{-1} (that is 6.5 to 1.2 μm). Thanks to this degree of freedom, the SEIRA sensing application was evaluated by enhancing several IR absorption lines of vanillin. The achieved enhancement factors are higher than 10^7 and perfectly matching the state-of-art of SEIRA. Ultimately, to improve the SEIRA readout, smaller gaps can be finely designed, offering larger near-field enhancement inside the gap region as we have proved theoretically. Such a stronger E-field intensity will in turn lead to a higher signal enhancement and thus to an extremely propitious sensitivity that goes one step forward to building compact and low-cost biosensing devices for sensitive IR detection based on the trendy Si-technology.

4. Experimental Section

FDTD Simulation: The electromagnetic response of the BT antenna integrated in a MIM configuration was simulated by 3D FDTD calculations using Ansys Lumerical 2021 R2.3 Finite difference solver. The structure was modeled as a 50 nm-thick aluminum (Al) BT with variable side length *L* and spacing *g*, on top of a 100 nm thick Al layer (mirror), with a 20 nm thick dielectric (SiO_2) layer stacked in between. For the Al, the dielectric constants reported in CRC Handbook of Chemistry & Physics by E. Shiles were referred to.[58] The SiO_2 material data were based on the Handbook of Optical Constants of Solids I–III by E. Palik,[59] but were slightly modified to match the real quality of the deposited material. An axiomatic refractive index equals to 1 (representing air) was maintained in the structure surroundings to create an asymmetric environment. Symmetric and anti-symmetric boundaries were employed along with *x* and *y* directions, and perfect matching layers (PMLs) along *z*-direction. A mesh grid of 2 nm was used around the tip-to-tip gap. An incident plane-wave was co-polarized (parallel to the BT axis) and launched backward along the *z*-axis for illumination. Thereafter, optical responses of Al-BT were collected using a monitor placed above the excitation source, so-called reflectance monitor. A field monitor was introduced in *xy*-plane to represent the electric field cartography. Throughout both monitors, the influence of geometrical parameters on the plasmonic behavior was studied.

Sample Fabrication: The main substrate constituted of HF-de-oxidized silicon (Si) wafer. 980 nm-thick SiO_2 layer was then deposited at 280 °C through Plasma-Enhanced Chemical Vapor Deposition (PECVD, CORIAL), followed by 100 nm of Al thermal deposition at 1 Å s^{-1}. 20 nm of SiO_2 was then sputtered at 0.4 Å s^{-1} using a plasma assisted sputtering machine (PLASSYS, sputtering system). The BT was tailored within the extent of 25×90 μm^2 by employing a Schottky-emitter field emission gun (FEG) EBL system (RAITH150 equipment) using a 7.5 μm aperture, operating at 20 kV (beam current of 20 pA), a working distance of 7 mm, and using an exposure stepsize of 2 nm. During exposure, the electron beam was intentionally scanned over the sample to define a matrix of 5×17 zones, in each of which triangle's side length *L* and gap *g* were fixed. After electron exposure, the exposed resist was developed in a Methyl Isobutyl Ketone (MIBK): 2-Propanol (IPA) solution (MIBK:IPA/1:3) for 45 s ensuring best profile for lift-off. After development, the sample was immediately rinsed in IPA (stopper solution) for 30 s. A 50 nm thick 99.99% pure aluminum layer was evaporated from tungsten boat (PLASSYS MEB550SL, electron-beam evaporation equipment) at a deposition rate of 2 Å s^{-1} in a 10^{-8} mbar vacuum chamber. Subsequently, lift-off process was performed in DMSO remover solution at 80 °C, followed by an ultra-sonication bath at 35 kHz for 60 s to guarantee a clean lift-off. The samples were thoroughly rinsed under deionized running water and blown with dry N_2. Following this process, nanostructure arrays consisting of two closely-placed equilateral triangles forming a BT shape with controlled side lengths and spacings were created.

Sample Characterization: RAITH150 imaging capability was used at 5 keV (beam current of 10 pA) to make calibrated images of the BT antennas. Imaging parameters (4×4 μm^2, 2000 points) lead to a resolution of 2 nm. The optical response of the fabricated resonators was characterized through a Hyperion 3000 microscope coupled to a FTIR spectrometer (Bruker Vertex 70). A broadband IR light source, namely Globar (silicon carbide SiC-based-MIR source) with potassium bromide (KBr) beam splitter was implemented for the measurements. The light was focused on the sample through a 36×/15× Cassegrain objectives (NA = 0.5/NA = 0.4) and collected onto a liquid N_2–cooled mercury cadmium telluride detector (MCT or Hg:Cd:Te) with a single element detector or with a focal plane array (FPA) of 64×64 pixels. The accessible spectral band was ranging between 400 to 8500 cm^{-1} and 800 to 3800 cm^{-1}, respectively. The acquired spectra were normalized to the spectrum of a gold mirror serving as background. Typically, background and spectral measurements were systematically executed using single element and FPA configurations with a resolution of 4 cm^{-1}, and interferograms from 1000 and 100 scans, respectively were averaged

to obtain one background-corrected spectrum, achieving a high signal-to-noise ratio. A co-polarized illumination was introduced (parallel to the BT main axis) as a 0° angle was red on the polarizer goniometer.

Acknowledgements

This work was done in collaboration with the LAAS-CNRS micro and nanotechnologies platform, a member of the Renatech French national network. M.N. acknowledges a doctoral grant from the National French Ministry for University Education, Research and Innovation. Partial fundings are acknowledged from the following projects: SEA (Occitanie French Region – ESR-PREMAT-238), EXTRA (ANR 11-EQPX-0016), NanoElastir (ASTRID 2020–2023), and ENVIRODISORDERS (MUSE UM 2021–2023). The authors acknowledge the technical work of the cleanroom staff (CTM), Frederic Pichot, Jean-Marie Peiris, and Renaud Felix. The authors thank Dr. Frank Neubrech for sharing his Eiler's smoothing program for the evaluation of SEIRA signals and Prof. Annemarie Pucci for the fruitful discussion. The authors thank Dr. Aude Mezy and Dr. Celine Schmitt for collaborating in the IR spectral lines interpretation.

Conflict of Interest

The authors declare no conflict of interest.

Data Availability Statement

The data that support the findings of this study are available from the corresponding author upon reasonable request.

Keywords

aluminum, infrared spectroscopy, localized surface plasmon resonance, metamaterials, plasmonic nanoantennas, surface-enhanced infrared absorption

Received: May 4, 2022
Revised: June 27, 2022
Published online: July 18, 2022

[1] G. Barbillon, *Materials (Basel)*. **2019**, *12*, 10.
[2] E. Ozbay, *Science (80-.)*. **2006**, *311*, 189.
[3] N. Jiang, X. Zhuo, J. Wang, *Chem. Rev.* **2018**, *118*, 3054.
[4] N. J. Halas, S. Lal, S. Link, W. S. Chang, D. Natelson, J. H. Hafner, P. Nordlander, *Adv. Mater.* **2012**, *24*, 4842.
[5] Y. B. Zheng, B. Kiraly, P. S. Weiss, T. J. Huang, *Nanomedicine* **2012**, *7*, 751.
[6] F. Wu, P. A. Thomas, V. G. Kravets, H. O. Arola, M. Soikkeli, K. Iljin, G. Kim, M. Kim, H. S. Shin, D. V. Andreeva, C. Neumann, M. Küllmer, A. Turchanin, D. De Fazio, O. Balci, V. Babenko, B. Luo, I. Goykhman, S. Hofmann, A. C. Ferrari, K. S. Novoselov, A. N. Grigorenko, *Sci. Rep.* **2019**, *9*, 20286.
[7] A. Ricciardi, A. Crescitelli, P. Vaiano, G. Quero, M. Consales, M. Pisco, E. Esposito, A. Cusano, *Analyst* **2015**, *140*, 8068.
[8] X. Han, K. Liu, C. Sun, *Materials (Basel)*. **2019**, *12*, 1411.
[9] J. Liu, M. Jalali, S. Mahshid, S. Wachsmann-Hogiu, *Analyst* **2020**, *145*, 364.
[10] C. Chen, J. Wang, *Analyst* **2020**, *145*, 1605.
[11] B. Špačková, P. Wrobel, M. Bocková, J. Homola, *Proc. IEEE* **2016**, *104*, 2380.
[12] A. W. H. Lin, N. A. Lewinski, J. L. West, N. J. Halas, R. A. Drezek, *J. Biomed. Opt.* **2005**, *10*, 064035.
[13] E. Kretschmann, H. Raether, *Z. Naturforsch. A: Phys. Sci.* **1968**, *23*, 2135.
[14] R. H. Ritchie, E. T. Arakawa, J. J. Cowan, R. N. Hamm, *Phys. Rev. Lett.* **1968**, *21*, 1530.
[15] P. Drude, *Ann. Phys.* **1900**, *306*, 566.
[16] S. A. Maier, H. A. Atwater, *J. Appl. Phys.* **2005**, *98*, 011101.
[17] F. Neubrech, C. Huck, K. Weber, A. Pucci, H. Giessen, *Chem. Rev.* **2017**, *117*, 5110.
[18] P. Biagioni, J. S. Huang, B. Hecht, *Rep. Prog. Phys.* **2012**, *75*, 024402.
[19] K. M. Mayer, J. H. Hafner, *Chem. Rev.* **2011**, *111*, 3828.
[20] A. E. Cetin, D. Etezadi, H. Altug, *Adv. Opt. Mater.* **2014**, *2*, 866.
[21] F. Neubrech, S. Beck, T. Glaser, M. Hentschel, H. Giessen, A. Pucci, *ACS Nano* **2014**, *8*, 6250.
[22] L. V. Brown, X. Yang, K. Zhao, B. Y. Zheng, P. Nordlander, N. J. Halas, *Nano Lett.* **2015**, *15*, 1272.
[23] A. Tittl, A. Leitis, M. Liu, F. Yesilkoy, D. Y. Choi, D. N. Neshev, Y. S. Kivshar, H. Altug, *Science* **2018**, *360*, 1105.
[24] T. Taliercio, P. Biagioni, *Nanophotonics* **2019**, *8*, 949.
[25] M. J. Milla, F. Barho, F. González-Posada, L. Cerutti, M. Bomers, J. B. Rodriguez, E. Tournié, T. Taliercio, *Nanotechnology* **2016**, *27*, 425201.
[26] F. B. Barho, F. Gonzalez-Posada, M. J. Milla, M. Bomers, L. Cerutti, E. Tournié, T. Taliercio, *Nanophotonics* **2017**, *7*, 507.
[27] Z. Li, W. Wang, D. Rosenmann, D. A. Czaplewski, X. Yang, J. Gao, *Opt. Express* **2016**, *24*, 20472.
[28] J. Martin, J. Plain, *J. Phys. D: Appl. Phys.* **2015**, *48*, 184002.
[29] B. Cerjan, X. Yang, P. Nordlander, N. J. Halas, *ACS Photonics* **2016**, *3*, 354.
[30] O. Lecarme, Q. Sun, K. Ueno, H. Misawa, *ACS Photonics* **2014**, *1*, 538.
[31] P. Arora, H. V. Awasthi, *Prog. Electromagn. Res. M* **2019**, *79*, 167.
[32] W. Li, K. Ren, J. Zhou, *TrAC, Trends Anal. Chem.* **2016**, *80*, 486.
[33] S. Dodson, M. Haggui, R. Bachelot, J. Plain, S. Li, Q. Xiong, *J. Phys. Chem. Lett.* **2013**, *4*, 496.
[34] B. Cerjan, N. J. Halas, *ACS Photonics* **2019**, *6*, 79.
[35] H. Wang, D. W. Brandl, P. Nordlander, N. J. Halas, *Acc. Chem. Res.* **2007**, *40*, 53.
[36] G. Q. Wallace, S. T. Read, D. M. McRae, S. M. Rosendahl, F. Lagugné-Labarthet, *Adv. Opt. Mater.* **2018**, *6*, 1701336.
[37] W. Ding, R. Bachelot, S. Kostcheev, P. Royer, R. Espiau De Lamaestre, *J. Appl. Phys.* **2010**, *108*, 124314.
[38] D. A. Rosen, A. R. Tao, *ACS Appl. Mater. Interfaces* **2014**, *6*, 4134.
[39] A. E. Cetin, S. Aksu, M. Turkmen, D. Etezadi, H. Altug, *J. Electromagn. Waves Appl.* **2015**, *29*, 1686.
[40] L. Li, S. Fang Lim, A. A. Puretzky, R. Riehn, H. D. Hallen, *Appl. Phys. Lett.* **2012**, *101*, 113116.
[41] L. Lin, Y. Zheng, *Sci. Rep.* **2015**, *5*, 14788.
[42] D. Ghindani, A. R. Rashed, H. Caglayan, *Photonics Res.* **2021**, *9*, 237.
[43] B. Wang, S. C. Singh, H. Lu, C. Guo, *Plasmonics* **2020**, *15*, 609.
[44] R. Nicolas, G. Lévêque, J. Marae-Djouda, G. Montay, Y. Madi, J. Plain, Z. Herro, M. Kazan, P. M. Adam, T. Maurer, *Sci. Rep.* **2015**, *5*, 14419.
[45] C. Valdez-Flores, M. P. Cañizares-Macias, *Food Chem.* **2007**, *105*, 1201.
[46] G.-A. Liu, R.-L. Zheng, *Pharmazie* **2002**, *57*, 852.
[47] V. Balachandran, K. Parimala, *Spectrochim. Acta, Part A* **2012**, *95*, 354.
[48] M. W. Knight, L. Liu, Y. Wang, L. Brown, S. Mukherjee, N. S. King, H. O. Everitt, P. Nordlander, N. J. Halas, *Nano Lett.* **2012**, *12*, 6000.
[49] K. M. Dorling, M. J. Baker, *Trends Biotechnol.* **2013**, *31*, 437.
[50] A. Hornemann, D. Eichert, S. Flemig, G. Ulm, B. Beckhoff, *Phys. Chem. Chem. Phys.* **2015**, *17*, 9471.

[51] P. Zucchiatti, G. Birarda, A. Cerea, M. S. Semrau, A. Hubarevich, P. Storici, F. De Angelis, A. Toma, L. Vaccari, *Nanoscale* **2021**, *13*, 7667.
[52] M. W. Knight, N. S. King, L. Liu, H. O. Everitt, P. Nordlander, N. J. Halas, *ACS Nano* **2014**, *8*, 834.
[53] A. Y. El-Etre, *Corros. Sci.* **2001**, *43*, 1031.
[54] P. H. C. Eilers, *Anal. Chem.* **2003**, *75*, 3631.
[55] J. Vogt, C. Huck, F. Neubrech, A. Toma, D. Gerbert, A. Pucci, *Phys. Chem. Chem. Phys.* **2014**, *17*, 21169.
[56] L. Dong, X. Yang, C. Zhang, B. Cerjan, L. Zhou, M. L. Tseng, Y. Zhang, A. Alabastri, P. Nordlander, N. J. Halas, *Nano Lett.* **2017**, *17*, 5768.
[57] G. Q. Wallace, H. C. Foy, S. M. Rosendahl, F. Lagugné-Labarthet, *J. Phys. Chem. C* **2017**, *121*, 9497.
[58] E. Shiles, T. Sasaki, M. Inokuti, D. Y. Smith, *Phys. Rev. B* **1980**, *22*, 1612.
[59] E. D. Palik, *Handbook of Optical Constants of Solids*, Academic Press, San Diego, CA **1991**.